

From conductance-based to integrate-and-fire modelling

Tomas Van Pottelbergh Guillaume Drion
Rodolphe Sepulchre

1 Abstract

This paper proposes a methodology to extract a low-dimensional integrate-and-fire model from an arbitrarily detailed conductance-based model. The method provides a computational bridge between the physiology of a neuromodulator at the cellular level and its impact in a possibly large neuronal network. The approach is illustrated on two well-documented examples of cellular neuromodulation: the transition between Type I and Type II excitability and the transition between spiking and bursting.

2 Introduction

Integrate-and-fire models have a long history, dating back to the beginning of the 20th century [22]. Because of their simplicity, they have long served as phenomenological models for action potential generation in neurons. Over the last few decades, the original Leaky Integrate-and-Fire model [14, 32, 20] has gradually been extended and modified to explain more neurological data and phenomena. Examples are the replacement of the linear function by a quadratic or exponential nonlinearity [9, 23, 11] and/or adding additional variables modelling the effects of refractoriness and adaptation [34, 26, 25, 30, 18, 2, 7].

With their increasing sophistication, integrate-and-fire models have become an attractive alternative to conductance-based models, since they are cheaper to simulate and more conducive to mathematical analysis.

Nevertheless, those advantages come with an important limitation: while they can reproduce various spiking patterns, they lack the physiological interpretation of a conductance-based model [33]. This is a severe obstacle when studying the role of cellular neuromodulation in a large network [5]. While

intrinsic neuromodulation is studied via changes of maximal conductances in conductance-based models, this is not evident to do in integrate-and-fire models without a biophysical connection.

The Multi-Quadratic Integrate-and-Fire (MQIF) model, presented in [7] and further studied in [33], is an example of such a model. Its variables have the interpretation of the membrane potential filtered in different timescales and its parameters relate to a local approximation of the balance between positive and negative conductance in each timescale. This model has been quite successful at capturing important modulation properties in a robust and qualitative manner.

The objective of the present paper is to provide a quantitative computational bridge between a detailed conductance-based model and its compact representation by a multi-scale integrate-and-fire model. Our motivation is to allow for a systematic mapping between the physiological parameters of a conductance-based model and the abstract parameters of its integrate-and-fire approximation.

We start by generalising the MQIF model to a multi-scale integrate-and-fire model in Section 3. The parameters of this integrate-and-fire model to be identified from the conductance-based model can be split into two groups. Section 4 discusses how to identify the ion current function of the integrate-and-fire model. The other parameters are treated in Section 5, which also discusses local optimisation to improve the result. We then apply this method to model modulation in two conductance-based models from the literature in Section 6. We end by discussing the limitations of the method and its connection other methods for the analysis of neural behaviour.

3 A multi-scale integrate-and-fire model structure

We consider a general multi-scale neuronal model of the form

$$C\dot{V} = I_{\text{app}} - I_{\text{ion}}(V, V_s, V_{us}, \dots) \quad (1)$$

$$\tau_s \dot{V}_s = V - V_s \quad (2)$$

$$\tau_{us} \dot{V}_{us} = V - V_{us} \quad (3)$$

...

The voltage equation (1) is the classical Kirchhoff relationship of a conductance-based model: the current I_{ion} is the total ionic current intrinsic to the cellular membrane composition. Its voltage-dependence is modelled through

the voltage variable V and lagged variables (V_s , V_{us} , \dots) that model the voltage filtered in distinct timescales (slow, ultraslow, \dots). Those variables differ from the gating variables of traditional conductance based models, but closely relate to the equivalent potentials originally defined in [19]. Note that the dynamics of those filters is chosen to be linear. The nonlinearity of the model is entirely concentrated in the scalar function I_{ion} , which we wish to choose to match the behaviour of a given conductance-based model.

When a reset is added to the multi-scale model, as in (4)–(6), the model is converted into an integrate-and-fire model. This simple integrate-and-fire model structure includes many models in the literature: the one-dimensional leaky, quadratic and exponential integrate-and-fire models, but also the multi-dimensional Izhikevich [18], AdEx [2], and Multi-Quadratic Integrate-and-Fire models [7, 33].

$$\begin{aligned}
 C\dot{V} &= I_{\text{app}} - I_{\text{ion}}(V, V_s, V_{us}, \dots) & \text{if } V \geq V_{\max} : \\
 \tau_s \dot{V}_s &= V - V_s & V \leftarrow V_r & (4) \\
 \tau_{us} \dot{V}_{us} &= V - V_{us} & V_s \leftarrow V_{s,r} & (5) \\
 & \dots & V_{us} \leftarrow V_{us} + \Delta V_{us} & (6)
 \end{aligned}$$

In the remainder of this paper, we concentrate on the integrate-and-fire version of the model. The reader should however be aware that there is a direct correspondence between the model (1)–(3) and the model (4)–(6) provided that the model (1)–(3) generates spikes. Each spike in the continuous-time model is replaced by a reset mechanism in the model (4)–(6). The motivation for this substitution is computational: the reset avoids the stiff integration of a spike, which can be a significant computational gain in the numerical integration of a large-scale spiking model. In contrast to models in the literature, we never manipulate the reset to generate solutions that would not be solutions of the continuous-time model (1)–(3). This constraint is key to retain a direct correspondence to the physiology of a conductance-based model.

A main property of the integrate-and-fire model (4)–(6) is that the nonlinear function I_{ion} only needs to be identified in the subthreshold voltage range $V < V_{\max}$.

4 Identification of the ion current function from a conductance-based model

We now develop a methodology to approximate a given conductance-based model by an integrate-and-fire model of the type (4)–(6). We make a distinction between the “structural” parameters of the model (the time constants and the reset parameters) and the single scalar nonlinear function I_{ion} . In this section, we determine I_{ion} for a given set of structural parameters. In the next section, we address the determination of the structural parameters and how the design can be optimised by iterating between the identification of the total ionic current and the identification of the structural parameters.

Given a conductance-based model and choice of structural parameters, we propose to identify the ionic current I_{ion} such as to optimise the matching between voltage-clamp experiments on the conductance-based model and on the integrate-and-fire approximation. We choose this criterion because it combines physiological relevance and computational tractability. It is physiologically relevant because conductance-based models are developed from voltage-clamp experiments in the first place. It is also computationally tractable because a voltage-clamp step response can be calculated in closed form both in a conductance-based model and in the integrate-and-fire model. In a conductance-based model, each gating variable obeys a differential equation of the form

$$\tau_{x_i}(V)\dot{x}_i = x_{i,\infty}(V) - x_i, \quad (7)$$

which becomes linear for a fixed value of V . The solution after a step from V_0 to V_{step} at $t = 0$ is described by

$$x_i(t) = x_{i,\infty}(V_0) + [x_{i,\infty}(V_{\text{step}}) - x_{i,\infty}(V_0)] \cdot [1 - e^{-t/\tau_{x_i}(V_{\text{step}})}], \quad (8)$$

assuming the membrane potential is at equilibrium at $t = 0$.

The response of the total ionic current I_{ion} in the conductance-based model to a voltage-clamp step is then obtained by direct substitution of $V(t) = V_{\text{step}}$ and $x_i(t)$ (given by (8)) in the expression for the total ionic current. The same calculation holds in the integrate-and-fire model (4)–(6) to obtain an expression of $I_{\text{ion}}(V(t), V_s(t), V_{us}(t), \dots)$.

The details of this simple idea are provided in the next sections.

4.1 Two-timescale models

We start by describing the method for conductance-based models that can be described well by a fast and slow timescale, which are well-separated ($\tau_s \gg \tau_f$). We consider a simple voltage clamp step experiment as in Figure 1,

stepping from the initial voltage V_s to the final voltage V . Assuming τ_f is a good approximation of the time constants of the fast gating variables, they will have approximately reached their steady-state value $x_{i,\infty}(V)$ at $t = 3\tau_f$. At the same time, because of timescale separation, the slow gating variables will not have significantly changed from their steady-state value $x_{i,\infty}(V_s)$.

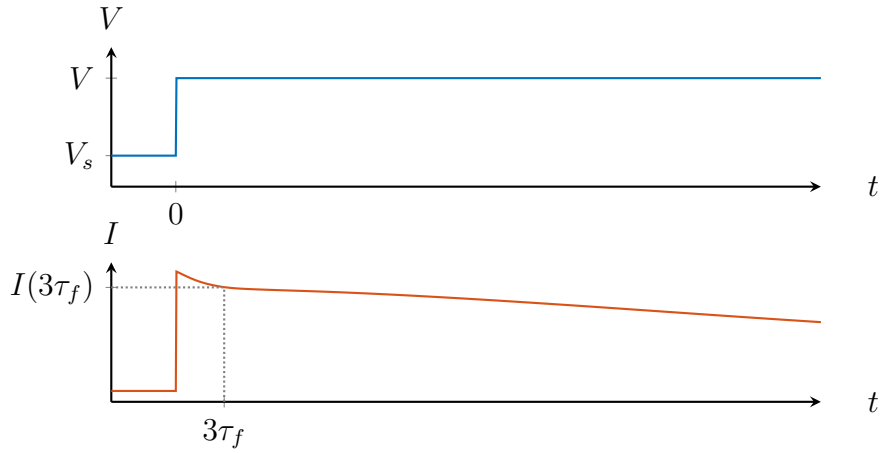


Figure 1: Voltage clamp step experiment on a two-timescale model. The voltage is stepped from V_s to V . The value of I at $3\tau_f$ will give a good approximation of $I_{\text{ion}}(V, V_s)$ of the multi-scale model.

In the multi-scale integrate-and-fire model, the fast dynamics are approximated as instantaneous, therefore the ion current immediately after a step from V_s to V is given by $I_{\text{ion}}(V, V_s)$. Therefore we can match this value to the solution of the voltage clamp step experiment on the conductance-based model at $t = 3\tau_f$. Using (8), this results in the expression

$$x_i = x_{i,\infty}(V_s) + [x_{i,\infty}(V) - x_{i,\infty}(V_s)] \cdot [1 - e^{-3\tau_f/\tau_{x_i}(V)}] \quad (9)$$

for each gating variable in the ion current equation of the conductance-based model.

This substitution thus makes $I_{\text{ion}}(V, V_s)$ of the integrate-and-fire model a function of the equations for the conductance-based model and the time constant τ_f . It is clear that in the limit of infinite timescale separation, the formula becomes a simple substitution of the fast and slow gating variables by their steady-state values at V and V_s respectively:

$$\lim_{\tau_{x_i} \rightarrow 0} x_i = x_{i,\infty}(V) \quad (10)$$

$$\lim_{\tau_{x_i} \rightarrow +\infty} x_i = x_{i,\infty}(V_s). \quad (11)$$

4.2 Three-timescale models

We apply the same idea to three-timescale models to find $I_{\text{ion}}(V, V_s, V_{us})$ as a function of the solution of a voltage clamp experiment. The simple procedure for two-timescale models cannot be used anymore, as it would always couple the slow and ultraslow voltage, and therefore only evaluate $I_{\text{ion}}(V, V_s, V_s)$. This can be resolved by devising a slightly more complex voltage clamp step experiment (see Figure 2): starting at V_{us} , stepping to V_s and finally to V after $3\tau_s$.

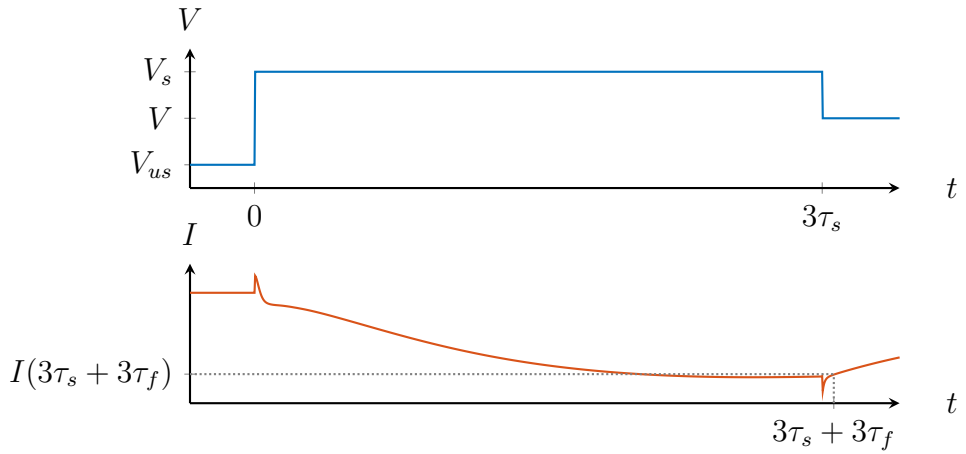


Figure 2: Voltage clamp step experiment on a three-timescale model. The voltage is stepped from V_{us} to V_s and then to V after $3\tau_s$. The value of I at $3\tau_s + 3\tau_f$ will give a good approximation of $I_{\text{ion}}(V, V_s, V_{us})$ of the multi-scale model.

Following the same reasoning as before, after $3\tau_s + 3\tau_f$ the fast gating variables will be approximately at their steady-state value $x_{i,\infty}(V)$. Similarly will the slow gating variables approximately be at the steady-state value $x_{i,\infty}(V_s)$, while the ultraslow gating variables will still be close to $x_{i,\infty}(V_{us})$. The value of the current at time $3\tau_s + 3\tau_f$ will therefore be a good approximation of $I_{\text{ion}}(V, V_s, V_{us})$ of the multi-scale model.

The necessary substitution for the gating variables in the ion current equation is given by

$$x_i = \bar{x}_i + [x_{i,\infty}(V) - \bar{x}_i] \cdot [1 - e^{-3\tau_f/\tau_{x_i}(V)}] \quad (12)$$

$$\bar{x}_i = x_{i,\infty}(V_{us}) + [x_{i,\infty}(V_s) - x_{i,\infty}(V_{us})] \cdot [1 - e^{-3\tau_s/\tau_{x_i}(V_s)}], \quad (13)$$

which is simply the solution of the gating variable equations at $t = 3\tau_s + 3\tau_f$ for the voltage clamp experiment shown in Figure 2. The limits for the

time constants going to zero and infinity are similar to those in the case of two-timescales:

$$\lim_{\tau_{x_i} \rightarrow 0} x_i = x_{i,\infty}(V) \quad (14)$$

$$\lim_{\tau_{x_i} \rightarrow +\infty} x_i = x_{i,\infty}(V_{us}), \quad (15)$$

while $x_i \approx x_{i,\infty}(V_s)$ if $\tau_{x_i} \approx \tau_s$ and $\tau_s \gg \tau_f$.

4.3 Pre-compensation of voltages in absence of timescale separation

The method in the previous sections assumes that each gating variable of the conductance-based model can be grouped into one of three categories: fast, slow, or ultraslow. Furthermore, the approximations rely on those timescales to be well separated from each other.

When the model does not show clear timescale separation, the assumption that the slower voltages will not significantly change after a step does not hold anymore. As long as the dynamics of the different gating variables can still be grouped in two or three timescales, it is possible to modify the described methods to compensate for the dynamics of the slower variables during the step experiment. In essence, the voltages used in the voltage clamp step experiments are modified so that the slower voltage(s) reach the desired values at the specified times $t = 3\tau_f$ (or $t = 3\tau_f + 3\tau_s$ for three-timescale models) the slower voltage(s) have reached the desired values. This is illustrated in Figure 3.

In the case of two timescales, only the initial voltage of the voltage clamp step needs to be changed. The value of V_s at $t = 3\tau_f$ can be computed given the initial voltage V_0 and the step voltage V :

$$V_s(3\tau_f) = V_0 + (V - V_0) (1 - e^{-3\tau_f/\tau_s}). \quad (16)$$

For this voltage to reach the desired value V_s^* at $t = 3\tau_f$, the above expression can be solved for V_0 :

$$V_0 = [V_s^* - V (1 - e^{-3\tau_f/\tau_s})] / e^{-3\tau_f/\tau_s}. \quad (17)$$

The same idea can be applied to three-timescale models, where V_{us} and V_s are now replaced by V_0 and V_{step} respectively. V_{step} is calculated in the same way as V_0 in the two-timescale case:

$$V_{\text{step}} = [V_s^* - V (1 - e^{-3\tau_f/\tau_s})] / e^{-3\tau_f/\tau_s}. \quad (18)$$

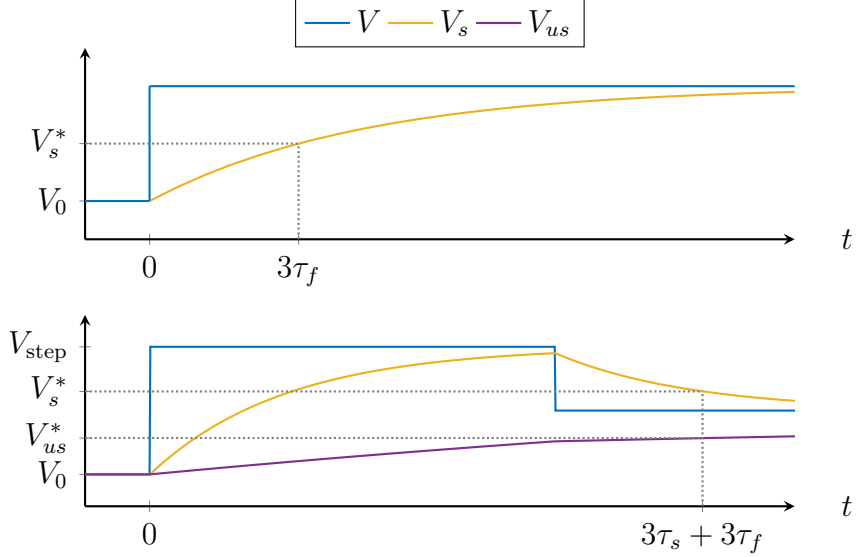


Figure 3: Illustration of the pre-compensation of step voltages to reach the desired values of the slow voltages at $t = 3\tau_f$ or $t = 3\tau_f + 3\tau_s$. Top: the choice of V_0 makes $V_s = V_s^*$ at $t = 3\tau_f$ for two-timescale models. Bottom: the choice of V_0 and V_{step} leads to $V_s = V_s^*$ and $V_{\text{us}} = V_{\text{us}}^*$ at $t = 3\tau_f + 3\tau_s$ for three-timescale models.

This can be done because V_s can be assumed to be at steady state at $t = 3\tau_s$. V_0 can then be computed using V_{step} . For simplicity, it is assumed that $\tau_{\text{us}} \gg \tau_f$, giving:

$$V_0 = [V_{\text{us}}^* - V_{\text{step}} (1 - e^{-3\tau_s/\tau_{\text{us}}})] / e^{-3\tau_s/\tau_{\text{us}}}. \quad (19)$$

If $\tau_{\text{us}} \gg \tau_f$ does not hold, the expression becomes slightly more complicated:

$$V_0 = [\bar{V} - V_{\text{step}} (1 - e^{-3\tau_s/\tau_{\text{us}}})] / e^{-3\tau_s/\tau_{\text{us}}} \quad (20)$$

$$\bar{V} = [V_{\text{us}}^* - V (1 - e^{-3\tau_f/\tau_{\text{us}}})] / e^{-3\tau_f/\tau_{\text{us}}}. \quad (21)$$

4.4 Calcium dynamics

Many conductance-based models also contain calcium-gated ion channels apart from the more common voltage-gated ion channels. The conductance of these channels is usually described by a (nonlinear) function of the calcium concentration instead of a product of gating variables. The calcium

dynamics obey a system of differential equations of the type

$$\tau_{[\text{Ca}^{2+}]}[\dot{\text{Ca}}^{2+}] = [\text{Ca}^{2+}]_{\infty}(V, x_{\text{Ca},i}, \dots) - [\text{Ca}^{2+}] \quad (22)$$

$$\tau_{x_{\text{Ca},i}}(V)\dot{x}_{\text{Ca},i} = x_{\text{Ca},i,\infty}(V) - x_{\text{Ca},i} \quad (23)$$

...

where $x_{\text{Ca},i}$ are the gating variables of the calcium channels. This will generally not result in a simple substitution expression. However, under the assumption that the calcium concentration changes much slower than the calcium gating variables, an approximate expression can be obtained. Assuming the calcium gating variables are at steady state whenever the voltage is constant during the voltage-clamp experiment, the expressions of the previous sections can be reused. $[\text{Ca}^{2+}](V_s)$ and $[\text{Ca}^{2+}](V)$ in these expressions are obtained by substituting the values of the calcium gating variables at $t = 3\tau_s$ and $t = 3\tau_s + 3\tau_f$ respectively. Because of its simplicity, this approximation will be used in the rest of this paper.

5 Iterative optimisation of the structural parameters

The previous section showed how to identify the function I_{ion} for a given set of structural parameters. In this section we discuss how to initialise those parameters and how to iteratively optimise them using current clamp data.

5.1 Initialisation of the time constants

To estimate the time constants, we assume that the conductance-based model can be described by the multi-scale model (1)–(3) in the subthreshold regime. This is of course an approximation, but allows to find a simple procedure to find an initialisation of the time constants.

In the integrate-and-fire model (4)–(6), the voltage-clamped relation from V to I_{app} has the classical structure of a parallel Wiener system, as shown in Figure 4. Note the additional voltage V_f , accounting for the dynamics of the fast ion channels. While this voltage will be merged with V in the final multi-scale model, it is necessary in order to find τ_f for the identification of I_{ion} .

This structure of parallel linear systems followed by a static nonlinearity can be exploited to estimate the time constants of the model. Applying a sufficiently small voltage clamp signal will reveal the dynamics of the linear

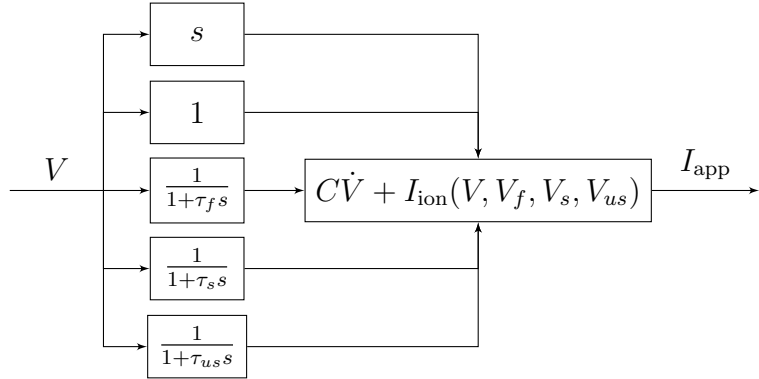


Figure 4: Block diagram representation of the multi-scale model (1)–(3) (extended with V_f) in voltage clamp. This is a parallel Wiener system with the linear systems on the left feeding into the nonlinearity on the right.

systems, since

$$I_{\text{app}} \approx C\dot{V} + \alpha_0 + \alpha_1 V + \alpha_2 V_f + \alpha_3 V_s + \alpha_4 V_{us}$$

$$\alpha_1 = \frac{\partial I_{\text{ion}}}{\partial V}, \alpha_2 = \frac{\partial I_{\text{ion}}}{\partial V_f}, \dots$$

where the coefficients α_i depend on the membrane potential around which the experiment is performed. The contribution of $C\dot{V}$ is easily removed as it only produces a sharp pulse at the time of the step. Repeating this experiment at multiple subthreshold voltages gives a more robust estimation, as some of the coefficients α_i might be small around a single voltage.

Classical system identification techniques can then be used to obtain the parameters of the linear systems from this voltage clamp data. We choose an extension by [27] of the Ho-Kalman-Kung algorithm [15, 35, 21] for step responses. The measured voltage clamp step responses are treated as the different outputs of the system to a single step input. The algorithm allows to select a model order (number of voltage variables) based on the Hankel singular values. The poles can also be restricted to be real and stable, to fit the structure of the multi-scale model. The sought time constants $\tau_f, \tau_s, \tau_{us}$ will hence be the negative inverse of the identified poles.

5.2 Initialisation of the other structural parameters

Apart from the time constants and I_{ion} , the only parameters left to identify in (4)–(6) are the membrane capacitance C , the reset parameters $V_r, V_{s,r}$ and ΔV_{us} , and the cutoff voltage V_{max} . Those parameters are easily estimated from current clamp simulations of the conductance-based model.

V_{\max} is taken to be just after the onset of the spike, around the maximum of the first derivative of the membrane potential. As long as V_{\max} lies sufficiently above threshold, its precise value should not influence the behaviour of the integrate-and-fire model. It is therefore fixed during the optimisation step.

The voltage reset V_r is always taken to be equal to V_{\max} . The reset values of the slower voltages are parameters to be optimised, but are physiologically constrained. A reasonable initialisation is to set $V_{s,r}$ sufficiently (e.g. 20 mV) above V_r . The parameter ΔV_{us} is constrained to be positive, since V_{us} would only increase after a spike in the model (1)–(3). Therefore it can be initialised at 0 mV.

Finally, the membrane capacitance C is initially set to 1 $\mu\text{F cm}^{-2}$, as is often the case in a conductance based model.

5.3 Local parameter optimisation

The structural parameters of the model can be iteratively optimised to improve the matching of representative current clamp data (see e.g. Figure 5, top).

We choose to minimise a cost function based on the residual current, which has been used before for the parameter estimation of conductance-based models [28, 17, 24]. The residual current for our model is defined as

$$I_{\text{res}} = C\dot{V} - I_{\text{app}} + I_{\text{ion}}(V, V_s, V_{us}) \quad (24)$$

and is zero when the membrane current equation is satisfied. The test data provides V and I_{app} , while the derivative \dot{V} can be obtained by numeric differentiation. The term I_{ion} depends on the chosen time constants and to evaluate it, the voltage trace is filtered by the corresponding first-order linear low-pass filters. The action potentials themselves are eliminated by removing the data for which $V > V_{\max}$, as the model is only optimised in the subthreshold regime. Instead, the different voltages are reset after every spike using their respective reset parameters, as shown in Figure 5 (bottom). The voltage traces of Figure 5 (bottom) can then be used to evaluate $I_{\text{ion}}(V, V_s, V_{us})$ and thus the residual current.

It was found that simple least-squares minimisation was sufficient for the purpose of this paper. Apart from the time constants, the free parameters in the optimisation are C and the reset values $V_{s,r}$ and ΔV_{us} . The advantage of using the residual current over the residual voltage for the cost function is that the former does not suffer from the extreme sensitivity to tiny variations in the spike timing. This can be observed in Figure 6: the cost function based

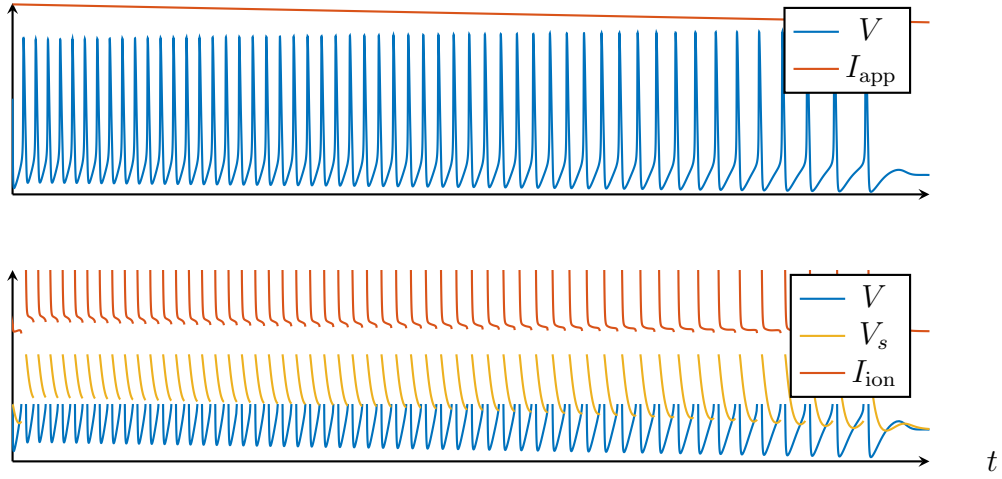


Figure 5: Test data generated using the Connor-Stevens model with $\bar{g}_A = 0 \text{ mS cm}^{-2}$. Top: Current clamp experiment with a decreasing ramp of the current I_{app} . Bottom: Data used to evaluate the cost function, where points for which $V > V_{\text{max}}$ are removed. V_s is obtained by filtering V with a first-order linear low-pass filter and reset to $V_{s,r}$ after every spike, and I_{ion} is evaluated using these V and V_s .

on the residual current is locally convex. In contrast, a cost function based on the residual voltage has many local minima and is much more irregular.

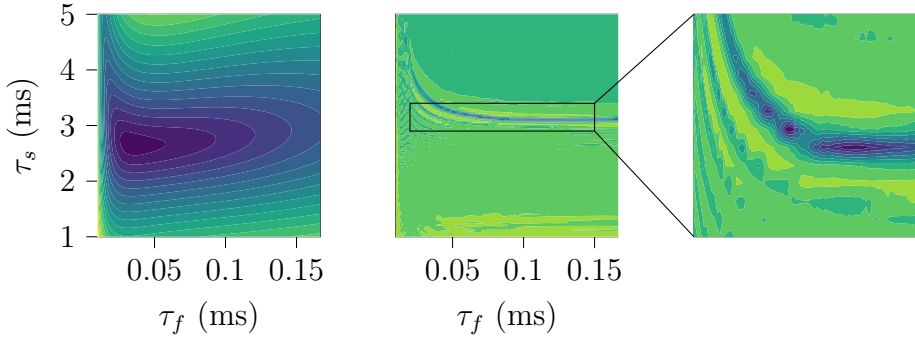


Figure 6: Contour plots of two least squares cost functions as a function of τ_f and τ_s for the Connor-Stevens model with $\bar{g}_A = 0 \text{ mS cm}^{-2}$. Left: cost function based on the residual current, as used in this paper. Centre & right: cost function based on the residual voltage ($V_{\text{res}} = V - V^*$, where V is the voltage of the test data and V^* is the voltage of the simulation of the integrate-and-fire model).

An important property of the multi-scale integrate-and-fire model is that its structural parameters have a clear interpretation. This makes it easy to initialise them at a reasonable value by inspection of a few voltage and current clamp experiments. The additional optimisation procedure is a straightforward least-squares local optimisation.

6 Integrate-and-fire modelling and phase portrait analysis

The benefit of the proposed integrate-and-fire model is not purely computational. We now show that it is also amenable to phase portrait analysis, which provides mathematical insight on the initial conductance-based model, regardless of its dimension.

For a two-timescale analysis, the phase portrait of the integrate-and-fire model is entirely characterised by two curves: the V -nullcline $I_{\text{ion}}(V, V_s) = I_{\text{app}}$, and the V_s -nullcline $V_s = V$. In other words, the level curves of the identified ion current I_{ion} determine the phase portrait of the model.

When the integrate-and-fire model is three-dimensional, we can describe its dynamics by considering the ultraslow variable V_{us} as a bifurcation parameter and by studying the family of phase portraits parameterised by V_{us} . In that sense, it can be said that the proposed integrate-and-fire model maps an arbitrary conductance-based model to a family of phase portraits. This is very convenient for a qualitative understanding of the dynamical properties of the model.

The following sections will illustrate the identification procedure and the phase portrait analysis of the integrate-and-fire model. The model is identified on two conductance-based models from the literature. The first is the classical Connor-Stevens model, whose behaviour can be easily modulated by a change of maximal conductance. The second is the model by [5], exhibiting a switchable slow negative conductance.

6.1 Modulation of excitability type in the Connor-Stevens model

The Connor-Stevens model [3, 4] is a six-dimensional conductance-based model for gastropod neuron somas. It has all the variables of the Hodgkin-Huxley model in addition to an extra potassium current I_A . One of its characteristic features is Type I excitability: the spiking frequency approaches zero when the applied current approaches the rheobase. This is in contrast to the

Type II excitability of the Hodgkin-Huxley model, whose spiking frequency makes a jump as the applied current is increased.

6.1.1 A two-timescale integrate-and-fire approximation of the Connor-Stevens model

Considering that this model was the example used by [19] for the equivalent potentials method, the method of this paper is expected to work well on this model. Similar to the work of Kepler et al., we start by a two-dimensional reduction of the model using the method of Section 4.1. The time constants found after the optimisation procedure are $\tau_f = 0.022$ ms and $\tau_s = 6.7$ ms. They reflect the timescale separation of the gating variables, which span a range of 0.03 ms to 3 ms.

The phase portrait of the two-timescale continuous-time model is displayed in Figure 7 (left). For a specific value of the applied current I_{app}^* , the V_s -nullcline intersects the V -nullcline at the transcritical singularity [12]. As the current increases from below to above the value I_{app}^* , stability is lost in a saddle-node on invariant circle (SNIC). This was shown to be the mechanism of Type I excitability in this model in [8]. The phase portrait of Figure 7 (right) shows the trajectory of spiking in the integrate-and-fire model (4)–(6) in orange. Since the model has a reset mechanism to replace the action potential generation, the periodic spiking occurs due to a hybrid limit cycle.

Figure 8 (top centre) illustrates the frequency-current (f-I) curves of the model. The bifurcation voltage is well predicted by the integrate-and-fire model. Although the onset of the f-I curve is sharper than for the original model, both curves eventually converge.

The excitability type of the model can be changed easily by modulating the maximal conductance \bar{g}_A . For $\bar{g}_A = 0$ mS cm⁻², the model is similar to the Hodgkin-Huxley model, which exhibits Type II excitability. We again obtain a two-timescale integrate-and-fire approximation of this model by finding I_{ion} and the structural parameters using the new value for \bar{g}_A . Its phase portrait is shown in Figure 8 (bottom left) and is qualitatively the same as that of the FitzHugh-Nagumo model [10, 29]. There is a subcritical Hopf bifurcation resulting in Type II excitability, confirmed by the f-I curve in Figure 8 (top left). The integrate-and-fire model loses stability at a slightly higher value of I_{app} than the original model, but both f-I curves remain close to each other afterwards.

On the other hand, increasing \bar{g}_A above its nominal value of 47.7 mS cm⁻² to 200 mS cm⁻² results in a bistable phase portrait (Figure 8, bottom right): for a specific range of I_{app} a stable hybrid limit cycle on the upper branch coexists with a stable fixed point on the lower branch of the V -nullcline. The

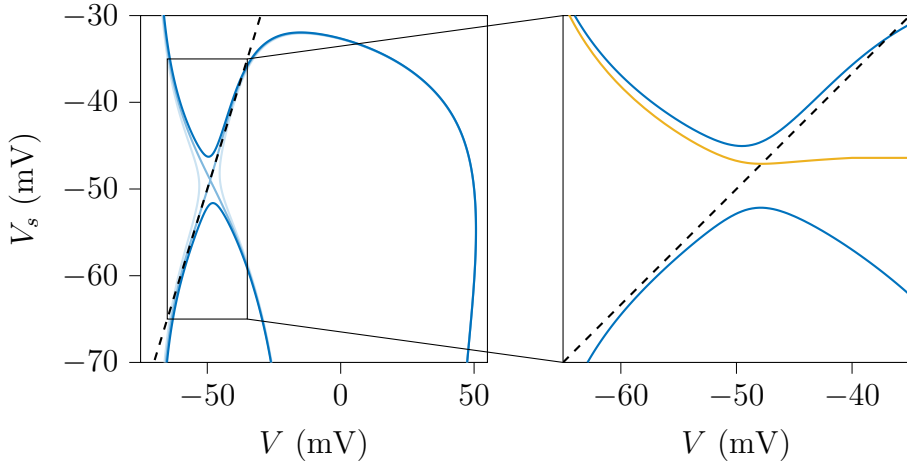


Figure 7: Phase portraits of the integrate-and-fire model obtained from the Connor-Stevens model with standard parameters [4]. The V - and V_s -nullclines are drawn as full and dashed lines respectively. Left: The V -nullclines are drawn for different values of I_{app} : low (light blue), I_{app} at the transcritical bifurcation in fast subsystem (medium blue) and high (dark blue). Right: The phase portrait for a high value of I_{app} , together with the stable (hybrid) limit cycle in orange.

fixed point loses stability in a saddle-node bifurcation, while the limit cycle disappears in a fold limit cycle bifurcation. This was called Type II* excitability in [8], which is similar to Type II excitability, but has a hysteretic f-I curve. Figure 8 (top right) shows that the integrate-and-fire model captures this hysteresis. Although the model starts spiking at a lower value of I_{app} , the saddle-node bifurcation occurs at the same point. This can be explained by the fact that the fold limit cycle bifurcation is a global bifurcation, which is harder to capture than the local saddle-node bifurcation.

6.1.2 A three-timescale integrate-and-fire approximation of the Connor-Stevens model

The results in the previous section show that the two-timescale reduction of the Connor-Stevens model neuron model is useful to obtain a qualitative approximation of the behaviour of the original model. The modulation of excitability type can be predicted from the phase portraits and it is possible to construct an integrate-and-fire model that replicates this modulation. However, the resulting integrate-and-fire model lacks a quantitative approximation of the voltage trace (not shown) and f-I curve. Kepler et al. improved

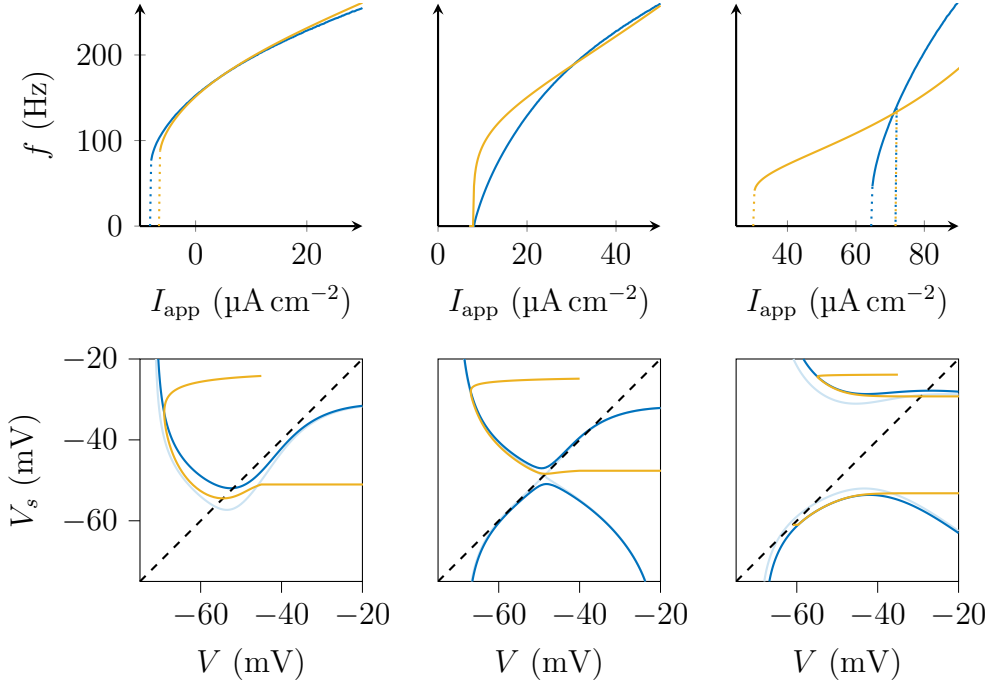


Figure 8: Phase portraits of the integrate-and-fire model (bottom) and f-I curves (top) of the Connor-Stevens model (blue) and the integrate-and-fire model (orange) for different values of \bar{g}_A . The V - and V_s -nullclines are drawn as full and dashed lines respectively, the trajectories after losing stability in orange. Left: $\bar{g}_A = 0 \text{ mS cm}^{-2}$, centre: $\bar{g}_A = 47.7 \text{ mS cm}^{-2}$, right: $\bar{g}_A = 200 \text{ mS cm}^{-2}$.

the quality of their reduction of the Connor-Stevens model by adding a third equivalent potential.

In an analogous effort, we approximate the original model by a three-timescale integrate-and-fire model using the method of Section 4.2. The three timescales are not strongly separated, however, and the method of Section 4.3 was used to adjust for this lack of separation. This resulted in a model with the time constants $\tau_f = 0.037 \text{ ms}$, $\tau_s = 1.7 \text{ ms}$ and $\tau_{us} = 2.8 \text{ ms}$. It is hypothesised that, like in the equivalent potentials method, this third timescale is necessary to account for the dynamics of the inactivation variable of the current I_A which are different from those of the other gating variables. Figure 9 (right) shows that the f-I curve for this three-timescale model almost perfectly match that of the original model. A comparison of a current clamp simulation with a linearly increasing applied current for both models (Figure 9, left) reveals very similar voltage traces.

While the f-I curves match well for the three-timescale model with $\bar{g}_A =$

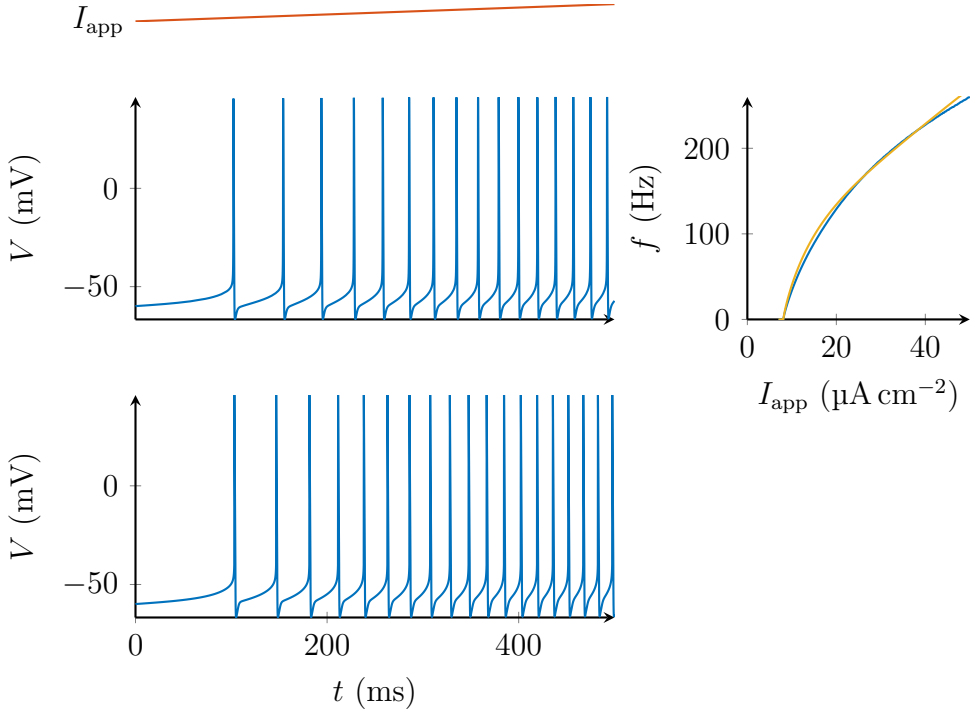


Figure 9: Left: voltage traces of the original Connor-Stevens model (top) and the three-timescale integrate-and-fire model (bottom) for I_{app} linearly increasing from 8 to 12 $\mu\text{A cm}^{-2}$. Right: f-I curves for the original Connor-Stevens model (blue) and the three-timescale integrate-and-fire model (orange).

47.7 mS cm^{-2} , we did not find a similar improvement for $\bar{g}_A = 200 \text{ mS cm}^{-2}$ (not shown). More work is necessary to determine whether the method is able to find a better approximation by using different current clamp data for the optimisation of the structural parameters.

6.2 Modulation between spiking and bursting due to a switchable slow negative conductance

Our second illustration uses the eight-dimensional conductance-based model introduced in [5]. A critical physiological feature of this model is a T-type calcium channel with low-threshold activation in the slow timescale. T-type calcium channels endow the model with slow regenerativity by having an activation which is slower than the sodium channel activation. Furthermore, the channels are inactivated at a relatively low threshold (on an even slower

timescale). This results in a slow negative conductance that is switchable by an external current: it is only switched on by hyperpolarisation. This current was hypothesised in [5] as a critical mechanism for the neuromodulation of network states. Figure 10 (left) shows how the switchable negative conductance can be observed from a voltage clamp step experiment. The slope of the current response in the slow timescale determines the absence or presence of slow regenerativity [13].

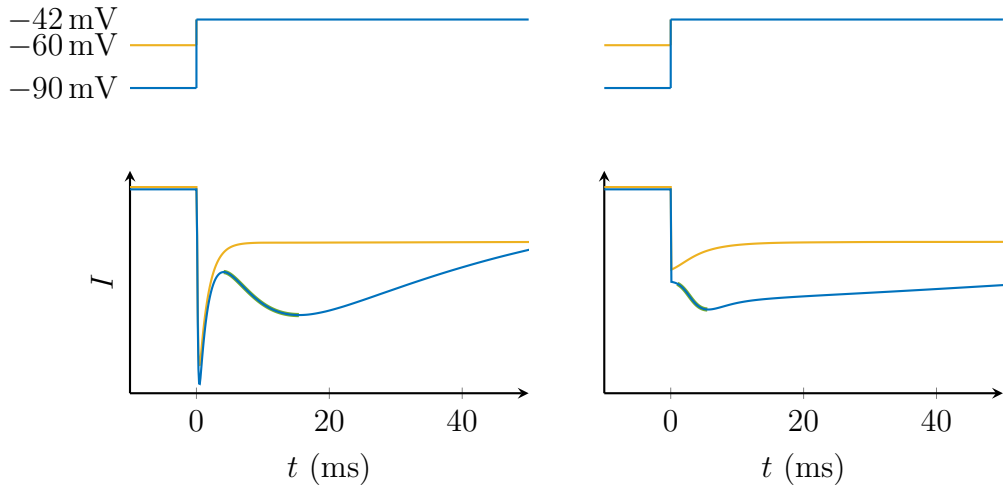


Figure 10: Comparison of the response to a voltage clamp step from a hyperpolarised (blue) and depolarised (orange) state for the original model of [5] (left) and its reduction (right). The voltage is stepped from -90 mV and -60 mV to -42 mV . The part of the responses highlighted in green shows the presence of a slow negative conductance in the hyperpolarised state and its absence in the depolarised state.

A distinctive behaviour of the model in current clamp is hyperpolarisation-induced bursting (HIB). This means the model can be switched from slow spiking to bursting by sufficiently lowering the input current, as shown in Figure 13 (top).

We use the method of Section 4.2 to construct an integrate-and-fire approximation of the conductance-based model of [5]. The calcium dynamics are treated as explained in Section 4.4. Its behaviour can be studied using three timescales. To visualise the obtained reduced model, phase portraits in the $V-V_s$ space are shown for different values of V_{us} . Assuming the ultraslow timescale is much slower than the slow timescale, the behaviour of the model can be analysed by looking at the fast-slow system in these phase portraits.

For $I_{\text{app}} = 0\text{ }\mu\text{A cm}^{-2}$, the original model shows regular spiking, with a

lower spiking frequency than during the bursting (Figure 11, left). As this is a two-timescale behaviour, V_{us} can be approximated by a constant value. Figure 11 (right) shows the phase portrait corresponding to this situation. There is no bistability between the resting and spiking state, and the phase portrait is the standard phase portrait of a spiking model.

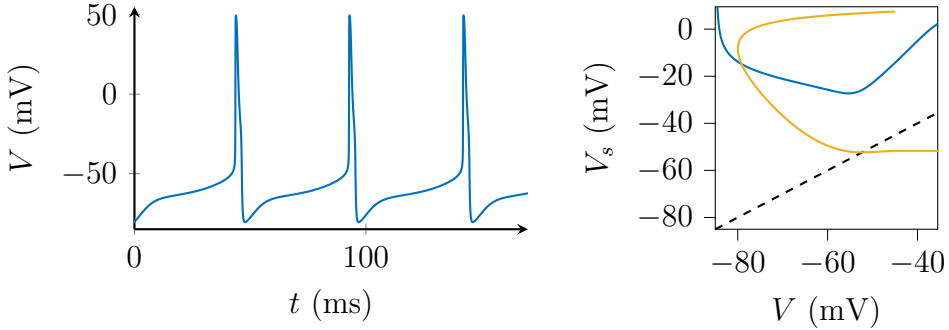


Figure 11: Left: Voltage trace of the model of [5] for $I_{app} = 0 \mu\text{A cm}^{-2}$. Right: Phase portrait of the three-dimensional integrate-and-fire approximation showing the absence of rest-spike bistability. The V - and V_s -nullclines are drawn as full and dashed lines respectively, the stable (hybrid) limit cycle in orange.

When the current is lowered to $I_{app} = -1.6 \mu\text{A cm}^{-2}$, the model bursts (Figure 12, top). The phase portraits during the different phases of the burst are shown in Figure 12 (bottom). The burst is initiated by the loss of stability in a saddle-node bifurcation on the lower branch of the V -nullcline (Figure 12, bottom left). The subsequent spiking, on the limit cycle on the upper branch of the V -nullcline, causes V_{us} to increase. This increase moves the two branches of the V -nullcline closer, resulting in bistability between a limit cycle and a stable fixed point (Figure 12, bottom centre). As V_{us} increases even further, the limit cycle is lost in a saddle-homoclinic bifurcation, moving the trajectory to the stable fixed point and thus terminating the burst (Figure 12, bottom right).

Figure 10 (right) shows the voltage clamp response of the reduced model for steps from two different voltages. Although different from the full conductance-based model of Figure 10 (left), the integrate-and-fire model retains the switchable negative conductance responsible for hyperpolarisation-induced bursting (HIB). Only for the hyperpolarised step, the slow response has a negative slope (highlighted in green). The fast response is instantaneous because V_f and V are a single variable in the reduced model.

Again, the obtained reduction can be used to construct an integrate-and-

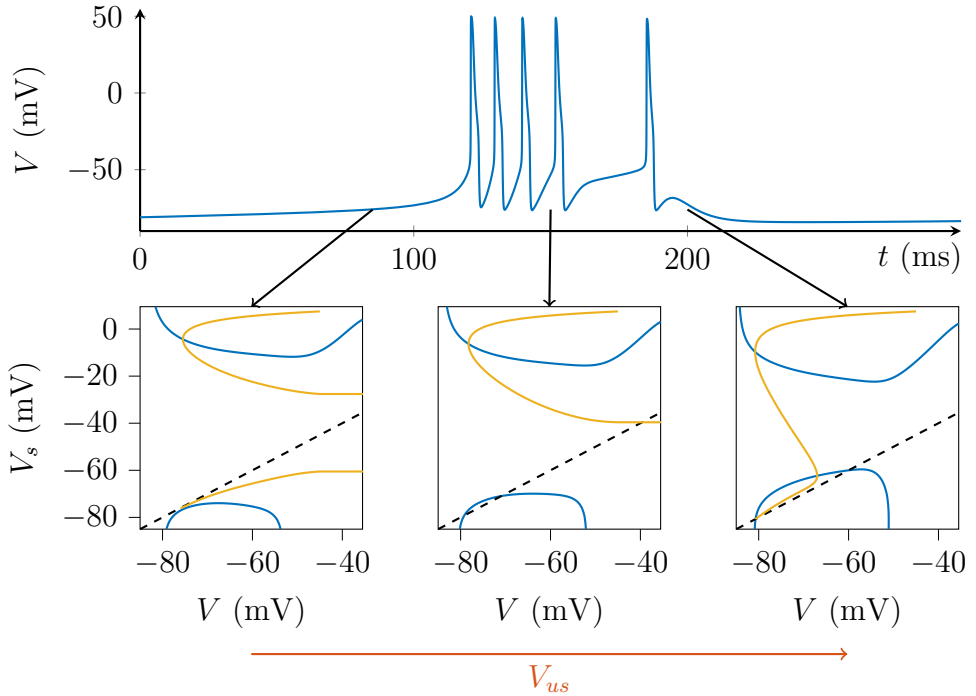


Figure 12: Top: Voltage trace of a burst in the model of [5] with $I_{\text{app}} = -1.6 \mu\text{A cm}^{-2}$. Bottom: Phase portraits of the three-dimensional integrate-and-fire approximation for different values of V_{us} showing the fast-slow system during different phases of the burst. The V - and V_s -nullclines are drawn as full and dashed lines respectively, the trajectories during a burst in orange.

fire model. Figure 13 shows the voltage trace before and after a hyperpolarising step current for the original model (top) and the reduced model (bottom). While the result is not a perfect quantitative match, it is quite accurate given the reduction for a reduction of the number of variables from eight to three.

7 Discussion

7.1 Validity of the method

The method of this paper attempts to match the voltage clamp response of an integrate-and-fire and conductance-based model. The idea of modelling the voltage clamp response to obtain a description of the neural dynamics is exactly what Hodgkin and Huxley did in their seminal work [16].

An important difference, however, is that we only match the response to a series of steps at a specific time. While this results in an analytical expression

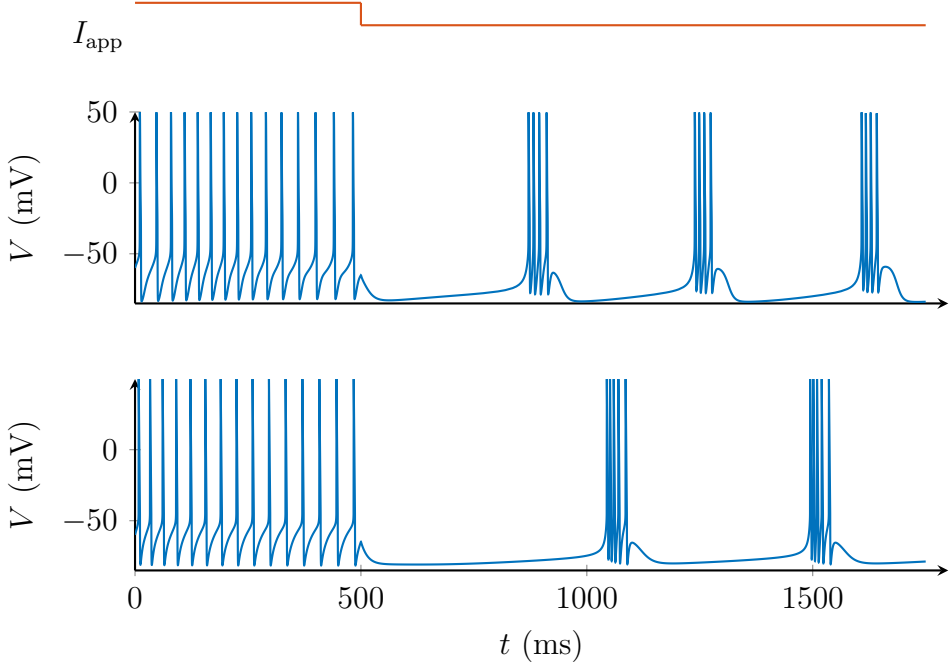


Figure 13: Voltage trace of the model of [5] (top) and its three-dimensional integrate-and-fire approximation (bottom) for I_{app} stepping from 0 to $-1.6 \mu\text{A cm}^{-2}$ at $t = 500 \text{ ms}$.

to reduce a conductance-based model, it also means that the voltage clamp response of both models will not necessarily match for other inputs and at other times. Nevertheless, under certain assumptions (explained below) the proposed method can be seen as a reduction method similar to the method of equivalent potentials of [19].

The notion of equivalent potentials is a way to convert the gating variables in a conductance-based model into potentials or voltages. Every variable x_i is simply replaced by the associated voltage of the steady-state function: $V_{x_i} = x_{i,\infty}^{-1}(x_i)$. In doing so, only the description of the system is changed, but not its input-output dynamics. The new form, however, can make it easier to discover relationships between different variables, necessary to reduce the system.

Kepler et al. propose such a reduction method by grouping equivalent potentials with similar dynamics and replacing them by a weighted average of their group. The weights are found by optimising the local approximation of the model. For the method to work, the dynamics of the equivalent potentials should fall into groups with similar dynamics. The method of this paper provides a simpler alternative based on voltage clamp experiments, by

making the additional assumption that the dynamics of each group of slower equivalent potentials can be described sufficiently well by a first-order linear low-pass filter as in (2)–(3), at least in the subthreshold regime.

This assumption might not always fully hold in practice, but the method can then still produce an acceptable reduction, although this should be carefully validated afterwards.

7.2 Local approximation by Multi-Quadratic Integrate-and-Fire model

The Multi-Quadratic Integrate-and-Fire (MQIF) model [7, 33] is a special case of the multi-scale integrate-and-fire model (4)–(6), in which I_{ion} is a sum of quadratic functions in V , V_s and V_{us} :

$$I_{\text{ion}}(V, V_s, V_{us}) = \bar{g}_f(V - V^0)^2 + \bar{g}_s(V_s - V_s^0)^2 + \bar{g}_{us}(V_{us} - V_{us}^0)^2. \quad (25)$$

The quadratics in V and V_s provide a normal form of the transcritical singularity in the fast subsystem, organising the rest-spike bistability. The quadratic in V_{us} models the ultraslow feedback necessary for bursting. The relative positions of the parameters V^0 and V_s^0 determine whether there is rest-spike bistability or not, but also influence the excitability type. This is illustrated in Figure 14, which sketches the phase portraits for the three possible regimes.

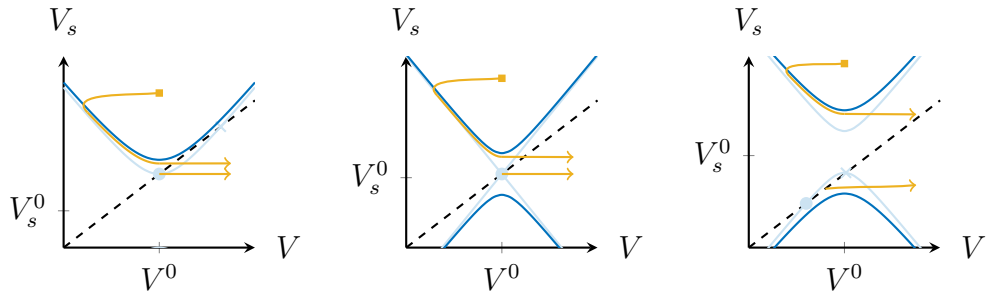


Figure 14: Modulation of the excitability type in the MQIF model. Changing V_s^0 in the MQIF model results in different types of excitability: Type II for $V_s^0 < V^0$ (left), Type I for $V_s^0 = V^0$ (centre) and Type II* [8] for $V_s^0 > V^0$ (right). The phase portraits show the V -nullclines just before (light blue) and after the bifurcation (dark blue). The V_s -nullclines are drawn as dashed lines. The stable fixed points are represented by filled circles, the saddle points by crosses. The possible trajectories are drawn in orange, with the reset points represented by squares.

We can regard the MQIF model as a local approximation of the model in the present paper around a transcritical singularity. This singularity is identified in the model (4)–(6) by finding the point (V^0, V_s^0) for which

$$\frac{\partial I_{\text{ion}}(V, V_s)}{\partial V} = \frac{\partial I_{\text{ion}}(V, V_s)}{\partial V_s} = 0, \quad (26)$$

together with the condition that the determinant of the Hessian at (V^0, V_s^0) should be negative (or zero, requiring further investigation). $I_{\text{ion}}(V^0, V_s^0)$ is then the current offset necessary to have the transcritical bifurcation occur at the same value of I_{app} . The values of \bar{g}_f and \bar{g}_s are simply the elements on the diagonal of the Hessian at (V^0, V_s^0) .

7.3 Connection to dynamic input conductances

The analysis method of this paper has some similarities with that of the dynamic input conductances (DICs) introduced in [6]. Both methods group the contributions of different ion channels into a fast, slow and ultraslow timescale. Nonetheless, a crucial difference between the methods is that the DICs are differential properties: they represent the change in current with an infinitesimal change in voltage. Instead, this paper considers the ion current itself as a function of voltages in different timescales. This is important because infinitesimal voltage clamp steps are hard to perform experimentally. In contrast, the voltage-clamp simulations considered in this paper could in principle be replaced by actual voltage-clamp experiments.

The other main difference between both methods is that DICs are defined around a steady state: all variables are at their steady-state value for the voltage V at which the DIC is calculated. The function $I_{\text{ion}}(V, V_s, V_{us})$ in this paper, on the other hand, allows the voltages in each timescale to be different, thus capturing the transient behaviour of the total ionic current. This is an important difference, because it allows the method of this paper to identify an integrate-and-fire neuron model, which is not possible from DICs.

While not identical, because of the way variables are divided over timescales, a property similar to DICs can be derived from $I_{\text{ion}}(V, V_s, V_{us})$ as follows:

$$g_f(V) = \left. \frac{\partial I_{\text{ion}}(V_f, V_s, V_{us})}{\partial V_f} \right|_{V_f=V_s=V_{us}=V} \quad (27)$$

$$g_s(V) = \left. \frac{\partial I_{\text{ion}}(V_f, V_s, V_{us})}{\partial V_s} \right|_{V_f=V_s=V_{us}=V} \quad (28)$$

$$g_{us}(V) = \left. \frac{\partial I_{\text{ion}}(V_f, V_s, V_{us})}{\partial V_{us}} \right|_{V_f=V_s=V_{us}=V}, \quad (29)$$

where g_f , g_s and g_{us} are the equivalent of the fast, slow and ultraslow DICs respectively. Since all voltages are taken as equal, it is clear that the DICs only reveal a subset of the information provided by $I_{\text{ion}}(V, V_s, V_{us})$.

7.4 Connection to I-V curve analysis

[31] propose a similar model of the total ionic current from I-V curves in different timescales. The main difference between the models is that the current functions in [31] are univariate. The current I_{ion} is then a sum of functions of V , V_s and V_{us} . The I-V curves are defined as the sum of all functions acting on their specific timescale and those faster, e.g. $I_f(V) + I_s(V)$ for the slow I-V curve.

8 Conclusion

This paper introduced a method to obtain an integrate-and-fire model from a conductance-based model, by matching voltage-clamp and current-clamp responses.

The proposed multi-scale integrate-and-fire model has a simple structure, but retains a close connection to the physiology of the conductance-based model.

The proposed method is applicable to arbitrary conductance-based models under the key assumption that the kinetics of the gating variables can be grouped in a few distinct timescales.

A Methods

A.1 Software

Simulations were performed in Python with the SciPy library using the equations stated in the text. Differential equations were solved using SciPy's backward differentiation formula (BDF) method. All figures were drawn using the Python packages Matplotlib and Tikzplotlib, and/or the L^AT_EX packages PGF/TikZ and PGFPLOTS.

A.2 Parameters of the conductance-based models

The parameters of the conductance-based models used in this paper take the original published values, except where a change of parameter is indicated. For the Connor-Stevens model [4] these are the following: $C =$

$1 \mu\text{F cm}^{-2}$, $\bar{g}_L = 20 \text{ mS cm}^{-2}$, $\bar{g}_{Na} = 120 \text{ mS cm}^{-2}$, $\bar{g}_K = 20 \text{ mS cm}^{-2}$, $\bar{g}_A = 47.7 \text{ mS cm}^{-2}$, $V_L = -17 \text{ mV}$, $V_{Na} = 55 \text{ mV}$, $V_K = -72 \text{ mV}$, $V_A = -75 \text{ mV}$. The parameters for the model of [5] are the means of the parameters used in their network simulations: $C = 1 \mu\text{F cm}^{-2}$, $\bar{g}_L = 0.055 \text{ mS cm}^{-2}$, $\bar{g}_{Na} = 170 \text{ mS cm}^{-2}$, $\bar{g}_{K,D} = 40 \text{ mS cm}^{-2}$, $\bar{g}_{Ca,T} = 0.55 \text{ mS cm}^{-2}$, $\bar{g}_{K,Ca} = 4 \text{ mS cm}^{-2}$, $\bar{g}_H = 0.01 \text{ mS cm}^{-2}$, $V_L = -55 \text{ mV}$, $V_{Na} = 50 \text{ mV}$, $V_K = -85 \text{ mV}$, $V_{Ca} = 120 \text{ mV}$, $K_D = 170$, $k_1 = 0.1$, $k_2 = 0.01$.

A.3 Parameters of the integrate-and-fire models

All simulations and phase portraits of the integrate-and-fire models are based on the published conductance-based model equations and parameters, unless stated otherwise in the text. The parameters of the integrate-and-fire models were found using the method described in Section 5, with SciPy’s Trust Region Reflective algorithm [1] for the least-squares optimisation. The current clamp test data was generated using linearly decreasing currents for the Connor-Stevens model and a hyperpolarising step current for the model of [5]. The data was sampled at 100 kHz and its transient was removed. The obtained values are given in Table 1 for each figure. The units of C , the time constants and the reset voltages are respectively $\mu\text{F cm}^{-2}$, ms, and mV.

Table 1: Parameters of the integrate-and-fire models.

Figure	C	τ_f	τ_s	τ_{us}	V_r	$V_{s,r}$	ΔV_{us}
7 & 8 (centre)	0.58	0.022	6.7		-40	-25	
8 (left)	0.86	0.03	3		-45	-24	
8 (right)	0.3	0.027	23		-35	-24	
9	1.2	0.037	1.7	2.8	-40	-20	0
10-13	0.82	0.89	4.3	278	-45	7.5	1.7

Acknowledgements

The authors would like to thank Ilario Cirillo, Thiago Burghi, Luka Ribar and Christian Grussler for the helpful discussions. TVP received a fees scholarship from the Engineering and Physical Sciences Research Council (<https://www.epsrc.ac.uk>) under grant number 1611337. Both TVP and RS were supported by the European Research Council (<https://erc.europa.eu>) under the Advanced ERC Grant Agreement number 670645. The funders

had no role in study design, data collection and analysis, decision to publish, or preparation of the manuscript.

References

- [1] M. Branch, T. Coleman, and Y. Li. A Subspace, Interior, and Conjugate Gradient Method for Large-Scale Bound-Constrained Minimization Problems. *SIAM Journal on Scientific Computing*, 21(1):1–23, Jan. 1999.
- [2] R. Brette and W. Gerstner. Adaptive Exponential Integrate-and-Fire Model as an Effective Description of Neuronal Activity. *Journal of Neurophysiology*, 94(5):3637–3642, Nov. 2005.
- [3] J. A. Connor and C. F. Stevens. Prediction of repetitive firing behaviour from voltage clamp data on an isolated neurone soma. *The Journal of Physiology*, 213(1):31–53, Feb. 1971.
- [4] J. A. Connor, D. Walter, and R. McKown. Neural repetitive firing: Modifications of the Hodgkin-Huxley axon suggested by experimental results from crustacean axons. *Biophysical Journal*, 18(1):81–102, Apr. 1977.
- [5] G. Drion, J. Dethier, A. Franci, and R. Sepulchre. Switchable slow cellular conductances determine robustness and tunability of network states. *PLOS Computational Biology*, 14(4):e1006125, Apr. 2018.
- [6] G. Drion, A. Franci, J. Dethier, and R. Sepulchre. Dynamic Input Conductances Shape Neuronal Spiking. *eNeuro*, 2(1), Mar. 2015.
- [7] G. Drion, A. Franci, V. Seutin, and R. Sepulchre. A Novel Phase Portrait for Neuronal Excitability. *PLoS ONE*, 7(8):e41806, Aug. 2012.
- [8] G. Drion, T. O’Leary, and E. Marder. Ion channel degeneracy enables robust and tunable neuronal firing rates. *Proceedings of the National Academy of Sciences*, 112(38):E5361–E5370, Sept. 2015.
- [9] B. Ermentrout. Type I Membranes, Phase Resetting Curves, and Synchrony. *Neural Computation*, 8(5):979–1001, July 1996.
- [10] R. FitzHugh. Impulses and Physiological States in Theoretical Models of Nerve Membrane. *Biophysical Journal*, 1(6):445–466, July 1961.

- [11] N. Fourcaud-Trocmé, D. Hansel, C. van Vreeswijk, and N. Brunel. How Spike Generation Mechanisms Determine the Neuronal Response to Fluctuating Inputs. *The Journal of Neuroscience*, 23(37):11628–11640, Dec. 2003.
- [12] A. Franci, G. Drion, and R. Sepulchre. An Organizing Center in a Planar Model of Neuronal Excitability. *SIAM Journal on Applied Dynamical Systems*, 11(4):1698–1722, Jan. 2012.
- [13] A. Franci, G. Drion, and R. Sepulchre. Robust and tunable bursting requires slow positive feedback. *Journal of Neurophysiology*, Dec. 2017.
- [14] A. V. Hill. Excitation and Accommodation in Nerve. *Proceedings of the Royal Society of London B: Biological Sciences*, 119(814):305–355, Feb. 1936.
- [15] B. L. Ho and R. E. Kalman. Editorial: Effective construction of linear state-variable models from input/output functions. *Automatisierungstechnik*, 14(1-12):545–548, 1966.
- [16] A. L. Hodgkin and A. F. Huxley. A quantitative description of membrane current and its application to conduction and excitation in nerve. *The Journal of Physiology*, 117(4):500–544, Aug. 1952.
- [17] Q. J. M. Huys, M. B. Ahrens, and L. Paninski. Efficient Estimation of Detailed Single-Neuron Models. *Journal of Neurophysiology*, 96(2):872–890, Aug. 2006.
- [18] E. M. Izhikevich. Simple model of spiking neurons. *IEEE Transactions on Neural Networks*, 14(6):1569–1572, Nov. 2003.
- [19] T. B. Kepler, L. F. Abbott, and E. Marder. Reduction of conductance-based neuron models. *Biological Cybernetics*, 66(5):381–387, Mar. 1992.
- [20] B. W. Knight. Dynamics of Encoding in a Population of Neurons. *The Journal of General Physiology*, 59(6):734–766, Jan. 1972.
- [21] S. Y. Kung. A new identification and model reduction algorithm via singular value decomposition. *12th Asilomar Conference on Circuits, Systems, and Computers*, pages 705–714, 1978.
- [22] L. Lapicque. Recherches quantitatives sur l’excitation électrique des nerfs traitée comme une polarisation. *Journal de Physiologie et de Pathologie Générale*, 9(1):620–635, 1907.

- [23] P. E. Latham, B. J. Richmond, P. G. Nelson, and S. Nirenberg. Intrinsic Dynamics in Neuronal Networks. I. Theory. *Journal of Neurophysiology*, 83(2):808–827, Feb. 2000.
- [24] N. F. Lepora, P. G. Overton, and K. Gurney. Efficient fitting of conductance-based model neurons from somatic current clamp. *Journal of Computational Neuroscience*, 32(1):1–24, Feb. 2012.
- [25] S. Mensi, R. Naud, C. Pozzorini, M. Avermann, C. C. H. Petersen, and W. Gerstner. Parameter extraction and classification of three cortical neuron types reveals two distinct adaptation mechanisms. *Journal of Neurophysiology*, 107(6):1756–1775, Mar. 2012.
- [26] S. Mihalas and E. Niebur. A Generalized Linear Integrate-and-Fire Neural Model Produces Diverse Spiking Behaviors. *Neural Computation*, 21(3):704–718, Oct. 2008.
- [27] D. N. Miller, J. Hulett, J. McLaughlin, and R. A. de Callafon. Thermal Dynamical Identification of Light-Emitting Diodes by Step-Based Realization and Convex Optimization. *IEEE Transactions on Components, Packaging and Manufacturing Technology*, 3(6):997–1007, June 2013.
- [28] T. M. Morse, A. P. Davison, and M. Hines. Parameter space reduction in neuron model optimization through minimization of residual voltage clamp current. In *Society for Neuroscience Abstracts*, volume 27, San Diego, CA, USA, Nov. 2001.
- [29] J. Nagumo, S. Arimoto, and S. Yoshizawa. An Active Pulse Transmission Line Simulating Nerve Axon. *Proceedings of the IRE*, 50(10):2061–2070, Oct. 1962.
- [30] C. Pozzorini, R. Naud, S. Mensi, and W. Gerstner. Temporal whitening by power-law adaptation in neocortical neurons. *Nature Neuroscience*, 16(7):942–948, July 2013.
- [31] L. Ribar and R. Sepulchre. Neuromodulation of Neuromorphic Circuits. *IEEE Transactions on Circuits and Systems I: Regular Papers*, 66(8):3028–3040, Aug. 2019.
- [32] R. B. Stein. A Theoretical Analysis of Neuronal Variability. *Biophysical Journal*, 5(2):173–194, Mar. 1965.
- [33] T. Van Pottelbergh, G. Drion, and R. Sepulchre. Robust Modulation of Integrate-and-Fire Models. *Neural Computation*, 30(4):987–1011, Jan. 2018.

- [34] U. Wehmeier, D. Dong, C. Koch, and D. Van Essen. Modeling the mammalian visual system. In C. Koch and I. Segev, editors, *Methods in Neuronal Modeling*, pages 335–359. MIT Press, Cambridge, MA, USA, 1989.
- [35] H. Zeiger and A. McEwen. Approximate linear realizations of given dimension via Ho’s algorithm. *IEEE Transactions on Automatic Control*, 19(2):153–153, Apr. 1974.